Available online at website: https://journal.bcrec.id/index.php/jcerp

Journal of Chemical Engineering Research Progress, 4 (1) 2027, 45-52

Original Research Article

Sensitivity Improvement of an In-Line Electromagnetic Metal Detector for Chemical Process Streams Using a Radial Basis Function Neural Network

Choljin O, Hyok Jo*, Gumhyok Pak, Jusong Rim, Boknam Huang, Cholryong Huang

University of Science, Department of Control Science, Pyongyang 355, Democratic People's Republic of Korea.

Received: 15th September 2026; Revised: 13th October 2026; Accepted: 26th October 2026
Available online: 19th November 2026; Published regularly: June 2027

Abstract

Tramp-metal contamination in chemical process streams damages crushers, mills, and extruders, degrades product purity, and can provide ignition sources in combustible-dust atmospheres. In-line electromagnetic induction (EMI) metal detectors are the standard countermeasure, but their practical sensitivity is limited by the product effect—the channel-correlated background signal produced by conductive or moist process materials—which forces conservative detection thresholds and causes false alarms or missed small fragments. This paper presents an in-line EMI metal detector whose sensitivity and false-alarm stability are improved by a radial basis function (RBF) neural network that estimates the size and cross-sectional position of a metallic fragment from the induced voltages of a six-coil array mounted on a process pipe. A prototype was dynamically validated over 200 passes with 125 metallic objects, achieving 99.2% detection accuracy and a 3 mm minimum detectable radius. Because the prototype's component-level documentation is no longer available, a fully parameterized simulation of the in-line configuration was conducted with representative design values and a product-effect model: on 2400 training and 1500 test samples, the RBF network matched a conventional amplitude-threshold detector at the nominal product level (AUC 0.949 versus 0.962) while a two-hidden-layer multilayer perceptron baseline performed comparably (AUC 0.945); the decisive advantage appeared under product-effect drift, where the false-alarm rate of the RBF detector rose to only 20.3% at 2.5× the nominal product level against 71.1% for the amplitude threshold, without recalibration. The RBF estimator also localized fragments with a mean absolute error of 2.0 mm (pipe radius 45 mm), an estimation capability the threshold detector does not provide. These results indicate that a lightweight trained estimator can substantially improve the operability of in-line metal detection in chemical plants.

Copyright © 2027 by Authors, Published by Universitas Diponegoro and BCREC Publishing Group. This is an open access article under the CC BY-SA License (https://creativecommons.org/licenses/by-sa/4.0).

Keywords: electromagnetic induction; product effect; sensitivity; radial basis function neural network; in-line instrumentation

How to Cite: O, C., Jo, H., Pak, G., Rim, J., Huang, B., Huang, C. (2027). Sensitivity Improvement of an In-Line Electromagnetic Metal Detector for Chemical Process Streams Using a Radial Basis Function Neural Network. *Journal of Chemical Engineering Research Progress*, 4 (1), 45-52. (DOI: 10.9767/jcerp.20856)

Permalink/DOI: https://doi.org/10.9767/jcerp.20856

1. Introduction

Tramp-metal contamination in chemical process streams, weld spatter, broken screen fragments, rust scales, and tool debris, damages crushers, mills, and extruders, degrades product purity, and can ignite dust explosions in combustible-dust atmospheres, so its removal is mandated as an explosion-protection measure [1–3]. Electromagnetic induction (EMI) detectors are the standard in-line countermeasure: a transmitter coil establishes an alternating field across a pipe and receiver coils sense the field scattered by eddy currents in a passing fragment [4,5]. Magnetic gradiometers and saturable-core magnetometers are alternative magnetic sensors with high sensitivity but demanding environmental compensation [6,7]. Physically, the scattered dipole field decays with $1/r^3$, so sensitivity to small fragments falls off rapidly, and

* Corresponding Author.
Email: jho9015@163.com (H. Jo)

continuous-wave implementations trade sensitivity against circuit simplicity [4,8]. Operationally, conductive or moist process materials (salt cakes, carbon blacks, catalyst pellets) generate a channel-correlated product-effect background that forces operators to raise detection thresholds, losing small-fragment sensitivity, or to tolerate false alarms that divert saleable product [1]. Conventional detectors additionally alarm on a single scalar amplitude and provide neither fragment size nor position, so contamination sources cannot be traced [4,5].

Reported remedies fall into three groups. Detector-design studies improve the front end through coil geometry and balanced receiver configurations that reject the common-mode product component at the circuit level [6,7]. Signal-processing and machine-learning studies replace scalar thresholds with estimators trained on the multichannel signals, where deep feedforward architectures provide universal approximation at higher training cost [9,10]; among these, radial basis function (RBF) networks with orthogonal-least-squares (OLS) center selection are attractive for embedded instruments because they train rapidly and deterministically and yield compact implementations [11–16], while deeper feedforward networks achieve comparable representational power at higher training cost [9], [10,19]. Quantitative nondestructive-evaluation studies, finally, demonstrate that material and defect properties can be estimated from measured field signatures rather than merely detected, which is precisely the information an operator needs for source tracing [21].

There is no published study, to the authors' knowledge, combines (i) a six-coil array whose median-based common-mode rejection suppresses the product effect at the signal level, (ii) a single-hidden-layer RBF estimator with OLS center selection that regresses fragment size and cross-sectional position from six induced voltages, and (iii) a quantified evaluation of false-alarm stability under product-effect drift with detection thresholds frozen at commissioning. Existing detectors either rely on scalar amplitude thresholds, which collapse under drift, or adopt model-based observers and multi-sensor fusion that require accurate plant models or additional hardware. This paper develops and evaluates exactly the combination of (i)–(iii) for 100 mm chemical-process pipes.

The objective of this study is therefore to improve the practical sensitivity and operability of in-line EMI metal detection in chemical plants. The contributions are: (a) a six-coil sensing array and analytical dipole model with median common-mode rejection; (b) an OLS-trained shallow RBF estimator for simultaneous size and position regression; (c) a Raspberry Pi 4 prototype with real-time visualization, networked event logging, and diverter output, dynamically validated over 200 passes with 125 metallic objects; and (d) a fully parameterized simulation quantifying false-alarm stability under product drift (20.3% versus 71.1% for the amplitude threshold at 2.5× nominal) with 2.0 mm localization accuracy.

The remainder of the paper is organized as follows. Section 2 presents the materials and methods: the coil layout and sensing-signal model, the RBF estimator, the prototype platform, and the simulation model and dataset. Section 3 reports the results and discussion: prototype validation, detection performance, robustness to product-effect drift, fragment localization, a comparison with previous studies, discussion and limitations with future work. Section 4 concludes the paper.

2. Materials and Methods

2.1 In-Line Coil Layout and Sensing-Signal Model

The detector is designed for horizontal mounting on a 100 mm-inner-diameter process pipe carrying powders, granules, or slurries (Figure 1). A transmitter (Tx) solenoid wound around the pipe (representative design: $N = 250$ turns, $I = 0.5$ A, length $L = 0.25$ m) establishes an approximately uniform axial excitation field $H_0 = NI/L = 500$ A/m in the bore. Six pickup coils of 8 mm radius are mounted flush with the inner wall at 60° angular spacing in a common cross-sectional plane, so that their sensitivity footprints partition the pipe cross-section into six sectors. When a metal fragment passes through the bore,

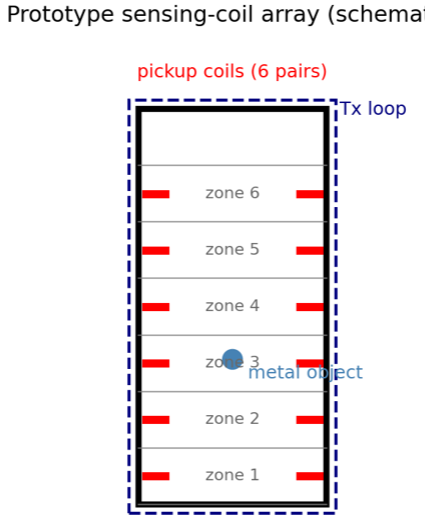


Figure 1. Sensing-coil array of the prototype: the transmitter loop and six pickup coils partition the aperture into six sensitivity zones; the drawing is a schematic of the dynamic-validation prototype.

Copyright © 2027, ISSN: 3032-7059

eddy currents induced in it create a secondary dipole field that couples most strongly to the nearest pickup coils.

The magnetic scalar potential of a closed current loop at distance r and angle θ to the dipole axis is approximated by the dipole potential:

$$\varphi_m = (P_m/4\pi r^2)\cos\theta \quad (1)$$

where $P_m = I \cdot S$ is the magnetic dipole moment, I the current, and S the enclosed area. Differentiating along the loop axis gives $H_{\mathrm{h}} = -\partial\varphi_{\mathrm{m}}/\partial\mathrm{h}$, and in cylindrical coordinates the axial field of a vertical dipole is:

$$H_h(\rho,h) = (P_m / 4\pi) \cdot (2h^2 - \rho^2) / (h^2 + \rho^2)\text{^}(5/2) \quad (2)$$

falling off as $1/r^3$. In the common cross-sectional plane ($h = 0$) of the pickup array, a fragment of radius a at position $q = (x, y)$ with induced dipole moment $m = 4\pi a^3 H_0$ induces in pickup coil i at position p_i the voltage:

$$V_i = \omega\,\mu_0\, m\, S_i / (4\pi\,|p_i - q|^3) + b + n_i \quad (3)$$

where ω = 2πf is the angular excitation frequency ($f = 10\,kHz$), S_i the pickup-coil area, b the product-effect background, and n_i electronic noise.

2.2 Product-Effect Rejection and Feature Preprocessing

The $1/r^3$ coupling concentrates the fragment signal on the nearest coils, whereas the product background b is common to all channels; this spatial contrast is the feature exploited by the estimator. As preprocessing, each six-channel vector is therefore median-centered in the linear domain, $d_i = V_i - median(V)$, which rejects the common product component while preserving the localized fragment signature, followed by the log-magnitude companding $z_i = sgn(d_i) \cdot log10(1 + |d_i|/V_0), V_0 = 1\,nV$, which equalizes the wide dynamic range. The product background is modeled statistically and its effect on detection is quantified in Section 3.3.

2.3 RBF Network Architecture and OLS Center Selection

Estimating the presence, size, and position of a fragment from the six pickup signals is a nonlinear classification-and-regression problem that conventional scalar-threshold electronics cannot solve. We construct and train a neural network built from radial basis functions (RBFs) [15].

An RBF network is a three-layer feedforward network that performs input–output mapping through radially symmetric activation functions [12]. The input layer distributes the six-dimensional feature vector:

$$X = (x_1, x_2, \ldots, x_n)^{\mathrm{T}},\ n = 6 \quad (4)$$

to the hidden layer. The j-th hidden unit computes the Euclidean distance to its center $C_j = (c_{j1}, \ldots, c_{jn})^{\mathrm{T}}$ and applies a nonlinear transformation:

$$u_j = \|\mathrm{X} - C_j\| = \sqrt{\left(\Sigma_{\mathrm{i}}(x_i - c_{ji})^2\right)} \quad (5)$$

$$\mathrm{z_j} = \mathrm{f(u_j)} = \exp\left(-\mathrm{u_j^2}/(2\sigma_{\mathrm{j}}^2)\right) \quad (6)$$

where σ_j is the width of the j-th basis function. The output layer produces a linear combination of the hidden activations:

$$y_k = \Sigma_{\mathrm{j}}\, w_{kj}\, z_j + w_{k0},\ k = 1, \ldots, L \quad (7)$$

The network has three outputs: the fragment-presence score and the two cross-sectional position coordinates. The implemented network is a three-layer, single-hidden-layer (shallow) RBF network: an input layer of $N = 6$ units, one hidden layer of M Gaussian RBF units whose centers C_j and widths σ_j are selected by the OLS procedure of Section 2.3, and an output layer of $L = 3$ linear units.

Taking all training samples as candidate centers, $C_i = X(i), i = 1, \ldots, N$, the hidden activation of candidate i on sample k is:

$$U_i(k) = exp(-\|X(k) - C_i\|^2 / (2{\sigma_i}^2)) \quad (8)$$

forming the design matrix $V = [B_1, B_2, \ldots, B_n]$ with $Bi = [U_i(1), \ldots, U_i(N)]^{\mathrm{T}}$. To rank candidates by their contribution to the target output, V is orthogonalized by Gram–Schmidt decomposition $V = QR$ with Q orthogonal and R upper triangular with unit diagonal, and each candidate is ranked by the error-reduction ratio [13]:

$$[err]_i = (q_{\mathrm{i}}{}^{\mathrm{T}} d)^2 / (\, q_{\mathrm{i}}{}^{\mathrm{T}} q_{\mathrm{i}} \cdot d^{\mathrm{T}} d\,) \quad (9)$$

with d the vector of desired outputs. Centers are selected sequentially in order of decreasing $[err]_i$ until the residual falls below a tolerance, which fixes M. The OLS procedure yields a compact, non-redundant hidden layer and improves generalization to weak fragment signals by reducing the variance of the learned mapping.

2.4 Output-Layer Training

With the centers fixed, the output weights $W = [w_{\mathrm{kj}}]$ are obtained in closed form as the

Copyright © 2027, ISSN: 3032-7059

(regularized) least-squares solution of the linear system (7) and may be refined by gradient-descent fine-tuning; for the squared error $E = \frac{1}{2}\Sigma k\ (d_k - y_k)^2$, the weight update follows the backpropagation rule [16]:

$$w_{kj}(t+1) = w_{kj}(t) - \eta \cdot \partial E/\partial w_{kj}, \partial E/\partial w_{kj} = -(d_k - y_k)z_j \quad (10)$$

The closed-form OLS initialization makes training deterministic and free of iterative convergence issues.

2.5 Prototype Embedded Platform

The sensing and estimation chain was implemented on a Raspberry Pi 4 running Linux, with detection, visualization, and communication software written in Python. Detection events are visualized in real time with OpenCV [17]: the active sector of the coil array is highlighted on an operator display with a color scale encoding the estimated fragment intensity. Every event is logged through an ODBC interface to a networked database together with its time stamp, estimated size and position, and detection intensity, and a query module supports retrieval by time, intensity, and event type. Multiple detection points along a process line can be organized into a local monitoring network, and a relay output actuates a diverter valve on detection. This embedded platform demonstrates that the trained estimator operates in real time on low-cost hardware.

2.6 Simulation Model and Dataset

To provide a reproducible, fully parameterized sensitivity analysis of the in-line configuration (Table 1), an electromagnetic model of the pipe detector was implemented according to Section 2. The product effect was modeled as a channel-correlated background $b = \sigma(\rho z + \sqrt{(1-\rho^2)}e)$, where z is common across channels, e is channel-independent, and $\rho = 0.75$ is the inter-channel correlation; σ varies with product composition and moisture. Training samples span the operating envelope $\sigma \in [60, 100]$ nV, electronic noise is 10 nV per channel, fragment radii are log-uniformly distributed over 0.5 – 8 mm, and fragment positions are uniformly distributed over the pipe cross-section ($r \leq 45$ mm). The dataset comprises 2400 training and 600 validation samples drawn across the envelope, plus 1500 test samples at the nominal product level $\sigma = 80$ nV; drifted test sets at $\sigma = 120, 160$, and 200 nV evaluate robustness to product variation. Detection and false-alarm performance are evaluated by ROC analysis [18]; all decision thresholds were fixed at the 1% false-alarm point on the nominal test set and never recalibrated. Three detectors were compared: the proposed RBF network, a conventional amplitude threshold on $\max|V_i|$ (the legacy industrial practice), and a two-hidden-layer multilayer perceptron (MLP, 64 and 32 ReLU units) trained by backpropagation [16,19] with scikit-learn [20], serving as a multilayer reference. Figure 2 shows the simulated field-sensor geometry and an example six-channel response for a 1 mm fragment at the pipe center.

3. Results and Discussion

3.1 Dynamic Validation

Because the component-level documentation of the prototype (exact winding counts and excitation frequency) is no longer available, the hardware is described at the system level in this paper, and the fully parameterized sensitivity analysis of the in-line configuration is provided by the simulation study in Section 2.6. Twenty operators carried metallic objects of different sizes through the sensing aperture for more than 200 passes, with ground truth recorded for every pass (object present or absent, size, and position). The detector outputs were compared against ground truth using detection accuracy, event-record accuracy, communication success rate, and minimum detectable size [18].

Table 1. Representative parameters of the in-line simulation.

Parameter	Value
Pipe inner diameter	100 mm
T_x solenoid field H_0	500 A/m (N = 250, I = 0.5 A, L = 0.25 m)
Excitation frequency f	10 kHz
Pickup coils	6, radius 8 mm, wall-mounted at 60° spacing
Electronic noise σ_n	10 nV/channel
Product background	$\sigma \in [60, 100]$ nV training; $\rho = 0.75$; nominal 80 nV
Drift test levels	120 / 160 / 200 nV
Fragment radius	0.5–8 mm (log-uniform)
Fragment position	uniform over cross-section, $r \leq 45$ mm
Train/validation/test	2400 / 600 / 1500 samples

Copyright © 2027, ISSN: 3032-7059

The estimator had been trained during commissioning on signal samples from the same test program as the evaluation passes. The 99.2% therefore characterizes the trained operating point of the prototype rather than generalization to unseen objects; this is stated as a limitation in Section 3.7. Table 2 summarizes the results. All 200 passes were registered; 124 of 125 metallic objects were correctly detected, a detection accuracy of 99.2%; the event-record accuracy was 98% and the communication success rate 99.8%. The minimum reliably detectable object was a sphere of 3 mm radius. These trials validate the complete sensing-and-estimation chain, including the estimator, visualization, and networked logging, under dynamic conditions.

3.2 Detection Performance at the Nominal Product Level

At the nominal product level, the three detectors are close, and the amplitude threshold is marginally ahead in pure detection: AUCs of 0.962 (threshold), 0.949 (RBF), and 0.945 (MLP) (Figures 3 and 4). The 90%-detection radius is approximately 1.2 mm for all three methods. This parity is an honest and expected result, when the product background is stationary, a well-set amplitude threshold extracts most of the available detection power, because the fragment signal adds to the background amplitude. The value of the trained estimator emerges under product variation (Section 3.3) and in estimation (Section 3.4).

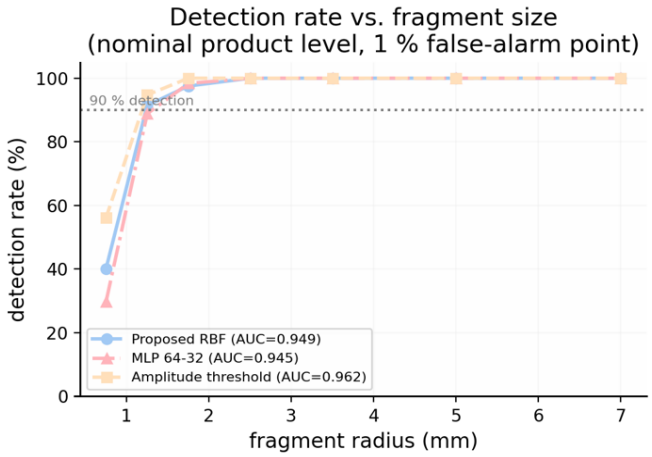


Figure 3. Detection rate versus fragment radius at the nominal product level (1 % false-alarm operating point): proposed RBF network, MLP baseline, and amplitude threshold.

Table 2. Dynamic validation results of the prototype detector.

No.	Metric	Ground truth	Result
1	Passes recorded	200	200
2	Metallic objects carried	125	124 detected
3	Detection accuracy	—	99.2 %
4	Event-record accuracy	—	98 %
5	Communication success rate	—	99.8 %
6	Minimum detectable size	—	3 mm (radius)

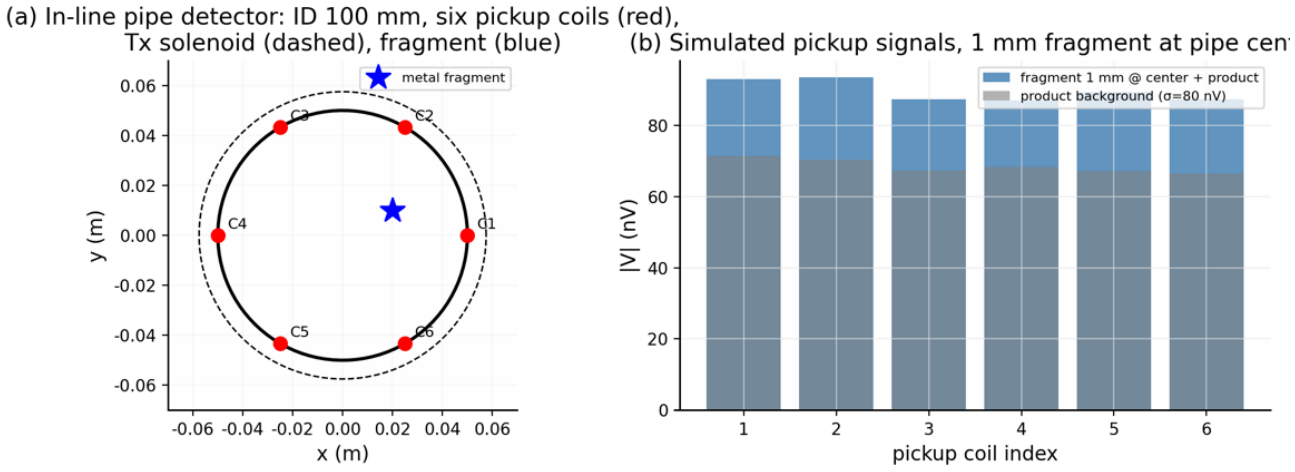


Figure 2. Simulation of the in-line configuration. (a) Pipe cross-section with six pickup coils (red), Tx solenoid (dashed), and a fragment (blue). (b) Simulated pickup signals for a 1 mm fragment at the pipe center superimposed on the product background (σ = 80 nV).

Copyright © 2027, ISSN: 3032-7059

3.3 Robustness to Product-Effect Drift

Figure 5 shows the false-alarm rate under product-effect drift with the decision thresholds fixed at the nominal 1% point. As the product background rises to 1.5× nominal, the false-alarm rate of the amplitude threshold climbs to 22.9%, more than one false alarm in five passes, whereas the RBF network remains at 6.8% (MLP 5.5%). At 2.5× nominal the false-alarm rate of the threshold reaches 71.1%, making continuous operation impossible without recalibration, while the RBF network stays at 20.3% (MLP 13.3%). The detection rates of the trained detectors degrade gracefully across the drift range (RBF true-positive rate 83.7% at 1.5× and 82.0% at 2.5×, against 96.0% and 96.7% for the threshold, which however operates at unusable false-alarm levels). This false-alarm stability is the decisive operational factor in chemical service: every false alarm diverts saleable product and may stop the line.

3.4 Fragment Localization

The RBF network regresses the fragment's cross-sectional position with a mean absolute error of 2.0 mm over the subset of test fragments of at least 1 mm radius (MLP: 2.2 mm; pipe radius 45 mm), i.e., approximately 5% of the pipe radius. The amplitude threshold provides no position estimate. In plant operation, this localization enables the source of contamination to be traced: successive detection points along a conveying line, each localizing the fragment within the pipe, narrow the search to a specific mill, screen, or valve.

3.5 Comparison with Previous Studies

Relating these results to the objectives, the trained estimator meets the two aims stated in the Introduction. First, practical sensitivity is preserved where conventional detectors fail: at a stationary product level our detector matches the amplitude threshold (AUC 0.949 versus 0.962), consistent with the understanding that a well-set threshold extracts most available detection power when the background is stationary [4], [5]; the advantage appears precisely under the condition that motivates this study, namely product-effect drift, where the threshold's false-alarm rate rises to 71.1% at 2.5× nominal while the RBF estimator remains at 20.3% without recalibration. This direction of improvement is consistent with quantitative nondestructive-evaluation practice, where detection decisions are strengthened by exploiting the full measured field signature rather than a scalar amplitude [21]. Second, the 2.0 mm localization capability has no counterpart in scalar-threshold practice and enables the source-tracing application described in Section 3.4.

Scientifically, the drift robustness is explained by the feature geometry rather than by capacity: the median-centered features remove the channel-correlated component that drifts with product composition, whereas the threshold operates on $\max|V_i|$, which is dominated by exactly that component. The comparison with the two-hidden-layer MLP (AUC 0.945; false-alarm rate 13.3% at 2.5×) indicates that the shallow RBF captures nearly all of the achievable structure, in agreement with the universal-approximation results for RBF networks [11] and their favorable bias–variance behavior when centers are selected by OLS [13]. We therefore interpret the residual gap to the MLP under drift as the price of a compact, deterministically trained embedded model.

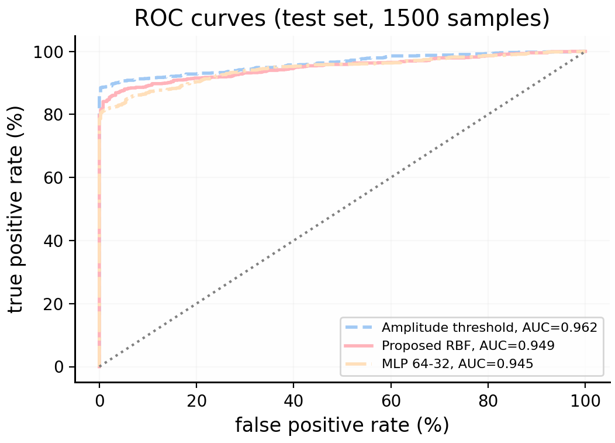


Figure 4. ROC curves on the 1500-sample nominal test set for the three detectors.

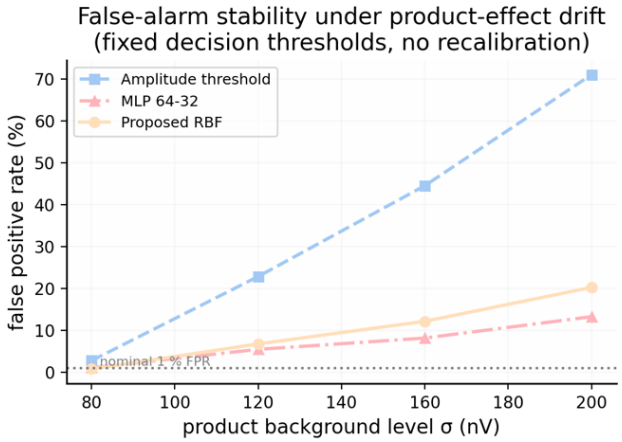


Figure 5. False-alarm stability under product-effect drift with fixed decision thresholds (no recalibration). The amplitude threshold's false-alarm rate explodes with the product level, whereas the trained estimators remain stable over the training envelope and degrade gracefully beyond it.

Copyright © 2027, ISSN: 3032-7059

3.6 Discussion

The prototype trials validate the complete sensing-and-estimation chain under dynamic conditions, and the simulation study separates the two effects that matter for chemical service: at a stationary product level, detection performance of the trained estimator and the amplitude threshold is comparable, with the threshold marginally ahead; under product-effect drift, the trained estimator's false-alarm stability is decisive.

3.7 Limitations and Future Work

Several limitations remain. First, the simulation uses representative rather than archived component parameters, so it demonstrates the mechanism and magnitude of the benefit rather than reproducing the prototype exactly; a follow-up with a fully documented production unit is needed. Second, the training envelope spans ±25% around the nominal product level; performance beyond the envelope (2–2.5× nominal) degrades and would require envelope-widening training data. Third, the product effect was modeled as stationary Gaussian background with fixed inter-channel correlation; real powders exhibit bursty, composition-dependent backgrounds that should be characterized on plant data. Fourth, the estimator was trained and evaluated on synthetic fragments; generalization to irregular fragments and to real product matrices remains to be quantified. Likewise, the prototype evaluation drew on a limited set of test objects; a fully independent evaluation on unseen objects remains future work. Deployment in classified (ATEX) atmospheres additionally requires certified enclosure and electronics [3]. Sensor fusion with complementary modalities such as microwave or millimeter-wave imaging [21] may address non-metallic contaminants. Finally, the logging of process and event data must comply with plant data-protection requirements [22,23]. Future work will address plant-data validation, envelope-widening training, and multi-point source-tracing networks.

4. Conclusion

This study set out to improve the practical sensitivity and operability of in-line EMI metal detection in chemical process streams, where the channel-correlated product effect forces conservative thresholds and frequent false alarms. The results answer this objective in three parts. First, the six-coil array with median common-mode rejection and the OLS-trained shallow RBF estimator were validated on a prototype under 200 dynamic passes with 125 metallic objects, achieving 99.2% detection accuracy and a 3mm minimum detectable radius on an embedded platform. Second, a fully parameterized simulation showed that the trained estimator preserves detection parity with the conventional amplitude threshold at the nominal product level while keeping the false-alarm rate at 20.3% versus 71.1% under 2.5× product-effect drift with frozen thresholds—the decisive operational advantage, since each false alarm diverts saleable product. Third, the estimator localizes fragments with 2.0mm mean absolute error, an estimation capability scalar-threshold detectors lack, enabling contamination-source tracing along a conveying line. These findings advance the field by demonstrating that a lightweight, deterministically trained estimator, rather than additional hardware, can convert multichannel EMI signals into drift-stable detection and localization for chemical plants. Applications include pneumatic-conveying lines, bulk-solids handling, and ATEX-classified environments (with certified enclosures), and extensions to microwave sensor fusion and networked multi-point source tracing are underway. Validation on plant data with real product matrices remains the principal open experiment.

Acknowledgement

This research did not receive any specific grant from funding agencies in the public, commercial, or not-for-profit sectors.

CRedit Authors Statement

Author Contributions: Choljin O: Conceptualization, Methodology, Software, Investigation, Writing – Original Draft. Hyok Jo: Conceptualization, Methodology, Formal Analysis, Writing – Review & Editing, Corresponding author. Gumhyok Pak: Investigation, Data Curation. Jusong Rim: Investigation, Visualization. Boknam Huang: Validation, Resources. Cholryong Huang: Supervision, Project Administration. All authors have read and agreed to the published version of the manuscript.

Declaration of Generative AI Use

During the preparation of this work, the authors used a generative AI assistant for language polishing and drafting assistance of parts of the revised text and for formatting the response to reviewers. All AI-assisted content was reviewed, verified, and edited by the authors, who take full responsibility for the accuracy, integrity,

Copyright © 2027, ISSN: 3032-7059

and originality of the published work. No experimental data, simulation results, or references were generated by AI tools.

References

[1] Mills, D. (2016). Pneumatic Conveying Design Guide (3rd ed.). Oxford, U.K.: Butterworth-Heinemann. DOI: 10.1016/C2014-0-02678-0

[2] Eckhoff, R.K. (2003). Dust Explosions in the Process Industries (3rd ed.). Amsterdam, The Netherlands: Gulf Professional Publishing. DOI: 10.1016/B978-0-7506-7602-1.X5000-8

[3] European Parliament and Council (2000). Directive 1999/92/EC on minimum requirements for improving the safety and health protection of workers potentially at risk from explosive atmospheres (ATEX). *Official Journal of the European Communities*, L 23, 57–64.

[4] Wait, J.R. (1971). Electromagnetic induction technique for locating a buried source. *IEEE Transactions on Geoscience Electronics*, 9(2), 95–98. DOI: 10.1109/TGE.1971.271473

[5] Das, Y., McFee, J.E., Toews, J., Stuart, G.C. (1990). Analysis of an electromagnetic induction detector for real-time location of buried objects. *IEEE Transactions on Geoscience and Remote Sensing*, 28(3), 278–287. DOI: 10.1109/36.54354

[6] Wynn, W.M., Frahm, C.P., Carroll, P.J., Clark, R.H., Wellhoner, J., Wynn, M.J. (1975). Advanced superconducting gradiometer/magnetometer arrays and a novel signal processing technique. *IEEE Transactions on Magnetics*, 11(2), 701–707. DOI: 10.1109/TMAG.1975.1058672

[7] Nabighian, M.N., Grauch, V.J.S., Hansen, R.O., LaFehr, T.R., Li, Y., Peirce, J.W., Phillips, J.D., Ruder, M.E. (2005). The historical development of the magnetic method in exploration. *Geophysics*, 70(6), 33ND–61ND. DOI: 10.1190/1.2133784

[8] Citak, H. (2020). Pulse induction metal detector: A performance application. *IEEE Transactions on Plasma Science*, 48(6), 2210–2223. DOI: 10.1109/TPS.2020.2996182

[9] Goodfellow, I., Bengio, Y., Courville, A. (2016). Deep Learning. Cambridge, MA, USA: MIT Press.

[10] LeCun, Y., Bengio, Y., Hinton, G. (2015). Deep learning. *Nature*, 521, 436–444. DOI: 10.1038/nature14539

[11] Park, J., Sandberg, I.W. (1991). Universal approximation using radial-basis-function networks. *Neural Computation*, 3(2), 246–257. DOI: 10.1162/neco.1991.3.2.246

[12] Bishop, C.M. (1995). Neural Networks for Pattern Recognition. Oxford, U.K.: Oxford University Press.

[13] Chen, S., Cowan, C. F. N., and Grant, P. M. (1991). Orthogonal least squares learning algorithm for radial basis function networks. *IEEE Transactions on Neural Networks,* 2(2), 302–309. DOI: 10.1109/72.80341

[14] Schwenker, F., Kestler, H.A., Palm, G. (2001). Three learning phases for radial-basis-function networks. *Neural Networks*, 14(4–5), 439–458. DOI: 10.1016/S0893-6080(01)00027-2

[15] Haykin, S. (2009). Neural Networks and Learning Machines (3rd ed.). Upper Saddle River, NJ, USA: Pearson.

[16] Rumelhart, D.E., Hinton, G.E., Williams, R.J. (1986). Learning representations by back-propagating errors. *Nature*, 323, 533–536. DOI: 10.1038/323533a0

[17] Bradski, G. (2000). The OpenCV library. Dr. Dobb's Journal of Software Tools.

[18] Fawcett, T. (2006). An introduction to ROC analysis. *Pattern Recognition Letters*, 27(8), 861–874. DOI: 10.1016/j.patrec.2005.10.010

[19] Hornik, K., Stinchcombe, M., and White, H. (1989). Multilayer feedforward networks are universal approximators. *Neural Networks*, 2(5), 359–366. DOI: 10.1016/0893-6080(89)90020-8

[20] Pedregosa, F., Varoquaux, G., Gramfort, A., Michel, V., Thirion, B., Grisel, O., Blondel, M., Prettenhofer, P., Weiss, R., Dubourg, V., Vanderplas, J., Passos, A., Cournapeau, D., Brucher, M., Perrot, M., and Duchesnay, E. (2011). Scikit-learn: Machine learning in Python. *Journal of Machine Learning Research*, 12, 2825–2830.

[21] Sheen, D.M., McMakin, D.L., Hall, T.E. (2001). Three-dimensional millimeter-wave imaging for concealed weapon detection. *IEEE Transactions on Microwave Theory and Techniques*, 49(9), 1581–1592. DOI: 10.1109/22.942570

[22] European Parliament and Council (2016). General Data Protection Regulation (GDPR), Regulation (EU) 2016/679.

[23] European Parliament and Council (2024). Artificial Intelligence Act, Regulation (EU) 2024/1689.

Copyright © 2027, ISSN: 3032-7059